Post-print

(final draft post-refereeing)

of

Multiscale modelling of MgO plasticity

J. Amodeo[1], Ph. Carrez[1], B. Devincre[2] & P. Cordier[1]

[1]Unité Matériaux et Transformations, UMR CNRS 8207, Université Lille 1, Cité Scientifique
59655 Villeneuve d'Ascq, France
[2]Laboratoire d'Etude des Microstructures, CNRS-ONERA, 29 avenue de la Division Leclerc
92322 Châtillon, France

Abstract:

We propose a multiscale model of plasticity of pure MgO single crystals. The core structure of the rate-controlling ½<110> screw dislocations has been modelled with the Peierls Nabarro Galerkin method. This model relies on γ-surfaces calculated *ab initio* for the {110}, {100} and {111} planes. The <110> screw dislocation spread mostly in the {110} planes. Its Peierls frictions are 150 MPa and 1.6 GPa for glide in {110} and {100} respectively. The kink-pair theory is applied to model thermal activation of dislocation glide over the Peierls barrier below the athermal temperature T_a and to built a velocity law in this regime. The critical resolved shear stresses are deduced below T_a from the Orowan law. Above T_a, the athermal stress τ_a is obtained from discrete dislocation dynamics simulations to account for dislocation-dislocation interactions. This model is found to reproduce satisfactorily the critical resolved shear stresses observed experimentally, provided the contribution of impurities (unavoidable in experiments) is subtracted.

Keywords : MgO, dislocations, Peierls Nabarro Galerkin model, thermal activation, dislocation dynamics simulations

1. Introduction

The Earth dissipates its internal heat to space through convection of the solid mantle which extends from 670 to 2900 km depth. It is thus a major concern in geophysics to understand how the mantle deforms. This issue is very challenging since mantle convection is associated with very high-pressure conditions (up to 135 GPa at the core-mantle boundary) and extremely low strain-rates (ca. 10^{-14} s^{-1}). (Mg,Fe)O is the second most important phase of the lower mantle (after (Mg,Fe)(Si,Al)O$_3$ perovskite). Understanding how this oxide deforms is thus critical to model flows in the mantle. In this perspective, several studies have been carried out recently to investigate the plasticity of (Mg,Fe)O or of MgO taken as a proxy of (Mg,Fe)O [1-5]. In most cases, experimental conditions were chosen such as to reproduce some of the characteristics of natural conditions (high-pressure, large strain rates, etc). However, despite significant progresses, experimental deformation under mantle conditions remains out of reach. Numerical modelling represents an alternative approach to investigate plasticity. A preliminary work in that direction [6] has shown the possibility of taking high-pressure conditions into account. The goal of the present study is to contribute to the development of this numerical approach.

In this paper, we will focus on plastic deformation of pure MgO at ambient pressure and under laboratory strain-rates. Indeed, MgO is a ceramic, stable at room pressure, for which a

large body of mechanical and microstructural data are available [7-11]. It is thus a good material to establish and verify our modelling approach. MgO is an ionic crystal with the rock-salt structure of space group $Fm\bar{3}m$. The easiest slip systems at ambient pressure are ½<110>{110} followed by ½<110>{100} (e.g. [12]) with a Burgers vector $b = 3$Å. Indeed, experimental studies show that the critical resolved shear stress (CRSS) for slip on {110} is an order of magnitude lower than on {100} [13,14]. Yield stresses, as in other ionic crystals, are sensitive to impurities contents [11,15]. Furthermore, both slip systems are characterized by a temperature dependence of CRSS believed to be governed by a Peierls mechanism (e.g. [16] or [17] and references therein).

At low temperature, the dislocation mobility is likely to be controlled by lattice friction which depends strongly on the fine structure of the core at the atomic scale [18]. Dislocation cores can be determined using either direct atomistic calculations [19-25] or based on the Peierls-Nabarro (PN) model [26-30]. At this stage, lattice friction is estimated through the Peierls stress which is often interpreted as the stress necessary to move a straight dislocation at 0K. For MgO, dislocation core structures have been modelled at the atomistic scale for the ½<110>{110} edge dislocation [31] or for the <100> screw dislocation [32,33]. More recently, the PN model has been applied to ½<110> dislocations [6,34].

To model plasticity, one needs to account for the thermally activated mechanism involved in dislocation motion at finite temperature, i.e. the kink-pair mechanism. Since the work of Seeger and Schiller [35], several approaches (among those we find the Line Tension model [36-40]) have been proposed to model kink-pairs mechanisms, including atomistic calculations [20,41-44]. Here, we propose to use the *elastic-interaction* model developed by Koizumi et al. [45,46] which has already been applied to MgO [47] and provides the stress dependence of the formation enthalpy for critical kink-pairs configurations.

Finally, a dislocation velocity law based on the kink-pair mechanism is introduced to calculate single crystal plastic properties. At low temperature, i.e. below a transition temperature (called the athermal temperature T_a), lattice friction is high. The plastic flow stress is mostly controlled by the dislocation mobility (and not by the forest obstacles). It is strongly thermally activated and can be described by the Orowan equation. Above T_a, lattice friction vanishes and gliding dislocations only face viscous drag. Plastic flow is therefore controlled by dislocations-dislocations interactions and is not thermally activated. Dislocation Dynamics (DD) simulations are very well adapted to describe this last regime [48-51]. In this study, DD is used below and above T_a.

In the next section, we will describe the simulation techniques used in the present work. The results of modelling are described in section III with a step-by-step discussion of the model progress. In section IV, the results of our multiscale model are critically discussed in comparison with experimental data.

2. Simulation techniques

2.1. Peierls-Nabarro Galerkin modelling of dislocation cores

Early models have been proposed for dislocation cores in MgO based on direct atomistic calculations (e.g. [31]). However, they were restricted to edge dislocation with little information on lattice friction. The use of the PN model has the advantage to give access to lattice friction in the form of the Peierls stress. Miranda and Scandolo [34] have proposed a first model of edge dislocations based on the PN model with results comparable to previous atomistic calculations [31]. In [6], similar calculations, extended to screw components, showed that the introduction of γ-surfaces calculated *ab initio* is a tool to incorporate the influence of pressure in the model. However, these calculations were intrinsically limited by the PN approximation of a planar core [29] and in [6], ½<110> screw dislocations were characterized by two distinct core structures depending on the glide plane. To solve this discrepancy and calculate more realistic dislocation core structures, one must use an extension of the PN model to account for multiple glide planes. Among the various possibilities [27, 52-54], we chose to use the Peierls-Nabarro Galerkin (PNG) method [55,56] which offers the possibility to calculate multiple glide planes and complex (possibly three-dimensional) cores. As in the initial PN model, the dislocation core structure is the outcome from the minimization of an elastic energy (through an approximation of a continuous field representation) and an interplanar potential derived from γ-surfaces calculations. γ-surfaces correspond to the excess energy per unit area due to a homogeneous shear along a given slip plane. γ-surfaces may thus capture the lowest energy paths available for dislocation core spreading. For the sake of clarity, let us describe the method by considering a unique slip plane Σ. In the PNG model, two distinct fields are used: $u(r)$ a three-dimensional displacement field of the volume V and a two-dimensional displacement discontinuity field $f(r)$ which is expressed in the normal basis of the Σ plane. Thus, $u(r)$ allows one to represent the continuous deformation around the dislocation core whereas f represents the displacement

jump when crossing Σ. The problem consists in minimizing the following energy E with respect to u and f:

$$E = \int_V \{E^e[u,f] - \frac{1}{2}\Omega\dot{u}^2\}dV + \int_\Sigma E^{isf}[f]d\Sigma \qquad (1)$$

where Ω corresponds to the material density. E^e corresponds to the elastic strain energy whereas E^{isf} is the inelastic stacking fault energy which depends on the material and controls the spreading of dislocation. E^{isf} is a function of the γ-surface energy from which all the linear elastic part has been subtracted [55]. Minimization with respect to f is achieved by means of a time dependent Ginzburg-Landau equation whereas an element free Galerkin method is used to compute the evolution of $u(r)$. In PNG calculations, once the equilibrium configuration of the dislocation core is reached, the finite elements cell can be strained in order to determine the Peierls stress. The latter corresponds to the critical applied stress for which a dislocation displacement made at 0K is irreversible in its glide plane.

2.2. Density functional theory (DFT) calculations of γ-surfaces

Following previous work [6], γ-surfaces calculations are based on supercells and are performed with the VASP code [57,58], based on the density functional theory (DFT). Calculations were performed within the Generalised Gradient Approximation (GGA) and using the all-electron Projector Augmented-Wave (PAW) method [59,60]. The outmost core radius for Mg and O atoms used in the simulation are 2.0 and 1.52 a.u respectively. Throughout this study, the first Brillouin zone was sampled using a Monkhorst-Pack grid and the electronic density is expanded on a plane wave basis set using a single cut-off energy of 500 eV assuring a convergence better than 10^{-3} meV per atom on the total energy. Extended details on those computations including the calculations of the unit cell parameter and the elastic constants can be found in [6]. The three supercells (of normal <100>, <110> and <111>) are built on a Cartesian reference frame defined by the normal of the stacking fault plane and by the shear direction. For the three supercells, a minimum of 16 atomic layers is used and external free surfaces are chosen to minimize possible spurious effect resulting from a dipolar field between charged surfaces. On top of that, a vacuum buffer is added in the direction normal to the slip plane to avoid interaction between the stacking faults replicas resulting from the use of periodic boundary conditions. The excess energies γ are calculated by imposing a given shear displacement value to the upper part of the supercell. During the calculations, all atoms but those located close to the buffer layer are allowed to relax in the directions perpendicular to the shear direction in order to minimize the energy of γ-surfaces.

2.3. Kink-pair modelling

As mentioned in the introduction, we propose to use the *elastic-interaction* model [45] to calculate the energy ΔH for kink-pair nucleation as a function of stress. From thermodynamics considerations, the rate of kink-pair nucleation is controlled by the free energy required to displace a critical dislocation segment into the next Peierls valley, however this energy can be approximated to the activation enthalpy when neglecting the associated entropy [61]. ΔH results from three contributions: the elastic interaction energy ΔE, the variation of the Peierls energy ΔP between a straight line and a kinked one and W, the work of the applied stress τ. Assuming a rectangular shape for the kink-pair configuration of height h and width w at low stress, the variation of enthalpy takes the form:

$$\Delta H = \Delta E + \Delta P - W \tag{2}$$

where the three terms depend on the couple of variable (h,w).

In Eq. (2), the formation of the kink-pair induces a variation ΔP that depends on the Peierls potential V_P as expressed in [45]. The work W is simply τbhw and for a screw dislocation, the variation of the elastic energy ΔE in case of isotropic materials [62] is given by Eq (3):

$$\Delta E(h,w) = \frac{\mu b^2}{2\pi} \left(\begin{array}{l} \sqrt{w^2 + h^2} - w - h + w\log\dfrac{2w}{w + \sqrt{w^2 + h^2}} \\ -\dfrac{1}{1-\nu}(w - \sqrt{w^2 + h^2} + h\log\dfrac{h + \sqrt{w^2 + h^2}}{w} - h\log\dfrac{h}{e\rho}) \end{array} \right) \tag{3}$$

where μ corresponds to the shear modulus, ν to the Poisson ratio and b to the Burgers vector of the dislocation. The elastic parameters μ and ν used are derived from the set of elastic constant proposed in [6]. The shear modulus μ is taken as 116.5 GPa and the Poisson ratio ν is deduced from anisotropic elastic parameter $K(\theta)$ (θ depending on the dislocation character). Assuming $K(0)=\mu$ for screws and $K(90)=\mu/(1-\nu)$ for edges, we used $\nu=0.18$ and 0.27 for {110} and {100} planes respectively.

In Eq. (3), ρ is a cut-off length. Fixing ρ is equivalent to choose an absolute energy of the dislocation [45,46]. Here following previous studies made with the *elastic-interaction* model [45, 47, 63], a value $\rho=0.05\zeta$ (ζ is to the half-width of the dislocation core) is considered. Based on expression of ΔE, ΔP and W, the critical shape (h^*,w^*) and critical enthalpy of the configuration ΔH^* can thus be calculated in the saddle point configuration as a function of stress τ.

2.4. Dislocation Dynamics (DD)

DD simulations have been performed using the open source simulation code mM (see [64] for a more specific description of the code). This simulation tool is a discrete three-dimensional dislocations dynamics code accounting for complex boundary conditions. Here, periodic boundary conditions are used in the calculations to model plasticity in bulk conditions [65,66]. As DD simulations and constitutive rules have been presented in several papers (e.g. [67,68]), we just recall here the basics of the technique. DD simulations with the mM code rely on a discretization of both space and time. For each slip systems, dislocation lines are discretized into a finite set of segments of fixed characters, screw, edge and mixed. Straight, glissile segments, are moved on a 3D cubic lattice exhibiting the lattice symmetry of MgO. To take into account the two possible slip systems families of MgO, ½<110>{110} and ½<110>{100}, the underlying lattice is composed of 96 elementary segments belonging to the 12 possible slip systems. The long-range interactions are treated using the Peach-Koehler formula. An effective resolved shear stress in the glide plane is calculated on each discretized segment, taking into account the stress field associated with the whole set of dislocation lines present in the simulated volume at each increment step, plus the applied stress accounting for the loading conditions, plus a line tension term accounting for the elastic energy lost when replacing locally curved dislocation sections by straight segments. Local rules are also prescribed to account for the contact reactions, such as annihilations or formation of junctions (see [69] or [70] and references therein). In response to the applied load, segments move with a velocity law which depends on the dislocation character. High mobility law are characterised by a velocity v simply proportional to stress whereas, in presence of lattice friction, mobility law are generally based on an Arrhenius form to account for the stress and thermally activated process [71-73, 79].

3. Results and discussion

3.1. From γ-surfaces to dislocation core structure

In MgO, previous calculations of Peierls stresses performed on ½<110> dislocations [6, 31, 34] suggest that, for both slip systems considered, Peierls stresses are lower for edge dislocations than for screw dislocations. The same conclusion is reached from the analysis of experimental results [16]. As a consequence, we will assume that plastic deformation is

governed by the mobility of screw dislocations and modelling at the elementary scale is performed on this character only.

γ-surfaces corresponding to {110}, {100} and {111} are presented on Fig. 1. ½<110> shear in {110} corresponds to the lowest energy path in agreement with previous calculations. Indeed, the maximum unstable stacking fault energy along <110> goes from 1.05 J/m^2 in {110} to 2.46 J/m^2 in {111}. In between we find 2.18 J/m^2 in {100}. No easier energy paths can be inferred from the γ-surfaces, even on {111} planes, where the stacking fault energy at 1/6<112> reaches 1.6 J/m^2 without displaying a clear minimum (corresponding to a potentially stable stacking fault).
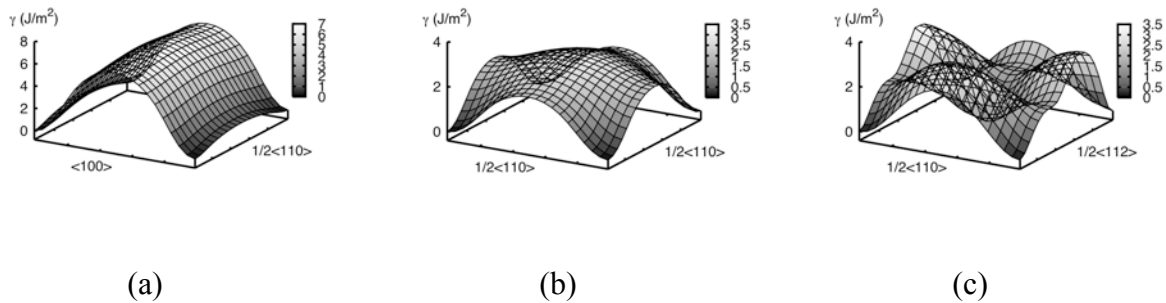

(a)   (b)   (c)

Fig. 1. γ-surfaces (in J.m^{-2}) calculated *ab initio* for {110} (a), {100} (b) and {111} (c).

To apply the PNG model, a node structure is built around the dislocation line with the symmetry of the crystalline structure. For a ½[110] Burgers vector, taken as an illustration, four possible families of plane must be considered $(1\bar{1}0)$, (001), $(1\bar{1}1)$ and $(1\bar{1}\bar{1})$. Within each family, several planes are superimposed in agreement with the crystal structure (Fig. 2a). A classical node resolution of 12 nodes per Burgers vector *b* has been used. One may note that increasing the resolution by a factor two did not affect the result. During the relaxation process, the dislocation core is allowed to spread in the four planes in response of the γ-surfaces. Between those planes, the medium exhibits a linear elastic behaviour. In the PNG calculation, the sheared plane associated with the dislocation line can be introduced horizontally or vertically in the finite element mesh, i.e. in different crystallographic planes. Whatever the sheared plane used to create the initial Volterra dislocation, its core is found to spread mostly in a {110} plane leading to the dislocation core structure shown on Fig. 2b. On the differential displacement map (Fig. 2b), only displacements along the Burgers vector are plotted since no edge components are observed. The size of the core and the amount of

Burgers vector density distributed in each plane can be evaluated using the disregistry function ϕ as presented on Fig. 3. Disregistry ϕ is closely linked to the f field used in PNG calculations. Indeed, f corresponding to a displacement jump, can be rewritten in a symmetrical form by removing the initial disregistry of $b/2$ and using a ϕ function [62]. Contrary to the initial PN model, ϕ can be recorded here along the γ-surfaces introduced in the calculation and as we cross the initial displacement, ϕ corresponds to the amount of Burgers vector distributed in each γ-surface plane. It appears that almost 80% of **b** is spread in {110} whereas less than 20% is found in {100}. Only a small residual part (below 1%) is found in the {111} planes.

Evaluations of the Peierls stresses have been done following the method presented in [56] by straining the simulation cell. As a consequence of the core structure, the Peierls stress is significantly lower in {110} than in {100}: 150 MPa for ½<110>{110} compared to 1600 MPa for ½<110>{100}.

As expected, PNG calculations lead to a single dislocation core structure for screw dislocations of ½<110> Burgers vector whatever the plane where the dislocation is introduced. The reason is that the core of the screw dislocation spreads mostly in {110} following the lowest energy path evidenced by γ-surface calculations. In a {110} plane, the half-width of the dislocation core is 3Å, a value which is slightly lower than previous evaluation of 4.4Å [6]. Realizing that the core that we calculate corresponds to a two-fold dislocation (only 80 % of b is spread in {110}), when classical PN calculations considers that the whole Burgers vector is distributed in the glide plane, the present work leads logically to a larger value of the Peierls stress than previously found in [6, 47]: 150 vs. 40MPa respectively. The present solution is likely to be more realistic since the dislocation core is better described and since the summation method used in [6, 47] to evaluate the Peierls stress is an approximation [28].
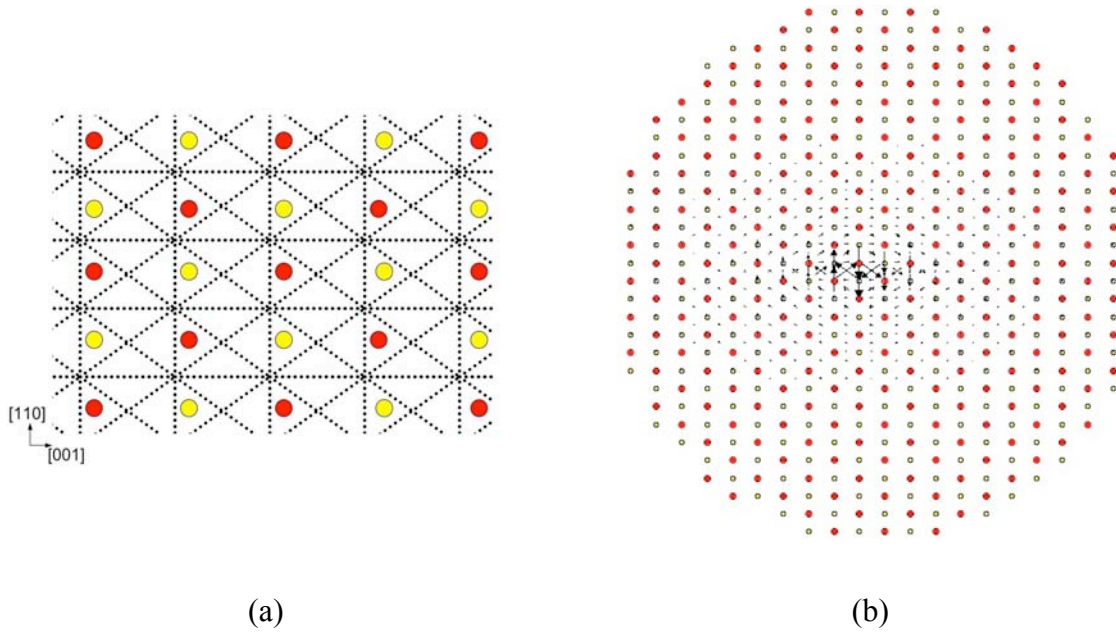
<center>(a)   (b)</center>

Fig. 2. (a) γ-surface positions used in the PNG simulations, superimposed on the MgO crystal structure view along [-110] (yellow and red atoms correspond respectively to Mg and O). (b) Differential displacement plot of the ½<110> screw dislocation as determined from PNG calculations (orientation identical to (a)). The largest displacement arrows reveal that most of the core is spread in the (110) plane.
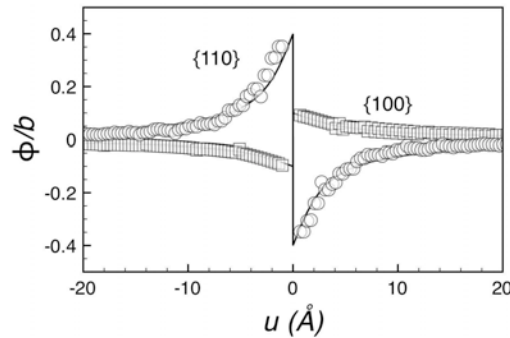

Fig. 3. Disregistry function $\phi(x)$ and $\phi(y)$ recorded respectively in {110} and {100} planes. $\phi(x)$, circle symbols, reachs an upper value of 0.4b whereas $\phi(y)$, square symbols, are limited to 0.1b (continuous lines represent a guide for eyes).

3.2. Kink-pair energy calculations

For the calculation of ΔP, we assume a sinusoidal Peierls potential V_P of periodicity a' (see Table 1) and parameterized with the Peierls stresses calculated above. Results of the calculation are presented on Fig. 4 and 5, with the evolution of the critical energy ΔH^* as a function of the applied stress on Fig. 5. $\Delta H^*(\tau=0)=\Delta H_0$ corresponds to twice the energy U_k of an isolated kink with a full height a'. Indeed, when τ approaches 0, the separation distance w^* of the kink pair is showed to increase considerably (Fig 4b), leading to a configuration where the interaction between kinks can be neglected. The values of ΔH_0 are given in table 1. As the

elastic-interaction model is restricted to the low stress regime [74], an extrapolation up to the Peierls stress has thus been performed using the classical formalism of Kocks et al. [75]:

$$\Delta H(\tau) = \Delta H_0 \left(1 - (\tau/\tau_P)^p \right)^q \tag{4}$$

In order to fit the empirical parameters p and q of Eq. (4), we used the saddle point energy ΔH^* (calculated at low stress) as well as the activation volume $V = bh^*w^*$ (Fig. 4a) that has been compared to the activation volume V given by the derivative of Eq. (4):

$$V(/b^3) = \frac{\Delta H_0}{b^3} (1/\tau_P) pq \left(\frac{\tau}{\tau_P} \right)^{p-1} \left(1 - \left(\frac{\tau}{\tau_P} \right)^p \right)^{q-1} \tag{5}$$

The fit of Eq. (4) is shown in dashed line on Fig. 5. Whatever the slip system, the critical widths w^* is found to decrease rapidly to an almost constant value for intermediate stresses (Fig. 4b).

	a''	τ_p (MPa)	ΔH_0 (eV)	p	q	w_c/b
½<110>{110}	$a/2$	150	1.14	0.5	2	113
½<110>{100}	$b/2$	1600	2.58	0.5	1	21

Table 1. Parameters related to the two slip systems considered in this study. *a'* is the periodicity of the Peierls potential; τ_p is the Peierls stress; ΔH_0 is the critical enthalpy for kink-pair nucleation under $\tau = 0$ GPa; p and q correspond to the empirical parameters of $\Delta H(\tau)$ in equation (4). w_c is the critical width of kink-pairs, here normalized by the Burgers vector modulus b.

In a recent critical review [17] of available experimental data on ionic compounds from literature, Takeuchi et al. concluded to an activation energy U_k around 0.3 eV for {110} which is close to our result: 0.55 eV. This value is in agreement with activation energies derived by measurement of Bordoni peaks which are in the range 0.2-1 eV, considering that these data are affected by small amounts of impurities [76]. It is more difficult to assess our value of U_k for {100} since Takeuchi et al. [17] proposed only a rough estimate (2 times lower than the value of Table 1) and since no measurement corresponding to {100} are available. However, the line tension model can also be used to calculate U_k. In that case, the energy of an isolated kink depends on a parameter E_0 corresponding to the energy of the dislocation in its ground state.

$$U_k \approx a' \sqrt{E_0 \frac{ba'\tau_P}{\pi}} \tag{6}$$

Assuming that E_0 should be mostly dominated by elastic energy [39], whatever the glide plane, E_0 could be considered independent of the glide plane and it turns out that the ratio between the two slip planes follows:

$$\frac{U_k^{\{100\}}}{U_k^{\{110\}}} \approx \sqrt{\left(\frac{b}{a}\right)^3 \tau_P^{\{100\}} \bigg/ \tau_P^{\{110\}}} \tag{7}$$

which is close to 2 and compares well with the ratio between ΔH_0 calculated here using the *elastic-interaction* model. Incidentally, this consistency validates our choice of the cut-off parameter ρ in Eq. (3).

The evolution of the kink-pair width w at low stress compares well with the Seeger and Schiller model [35]. Indeed, we checked that the kink-pair width (Fig. 4b) varies at low stress as a function of $1/\sqrt{\tau}$. We note finally that ½<110>{110} dislocations are characterized by wider kink-pairs compared to ½<110>{100} dislocations. This feature is strongly related to the value of σ_p/μ. Indeed, for slip systems with low Peierls stresses, or low Peierls potentials (which is here the case for ½<110>{110}), kink-pairs would be wider since the line tension governs the kink formation [77].
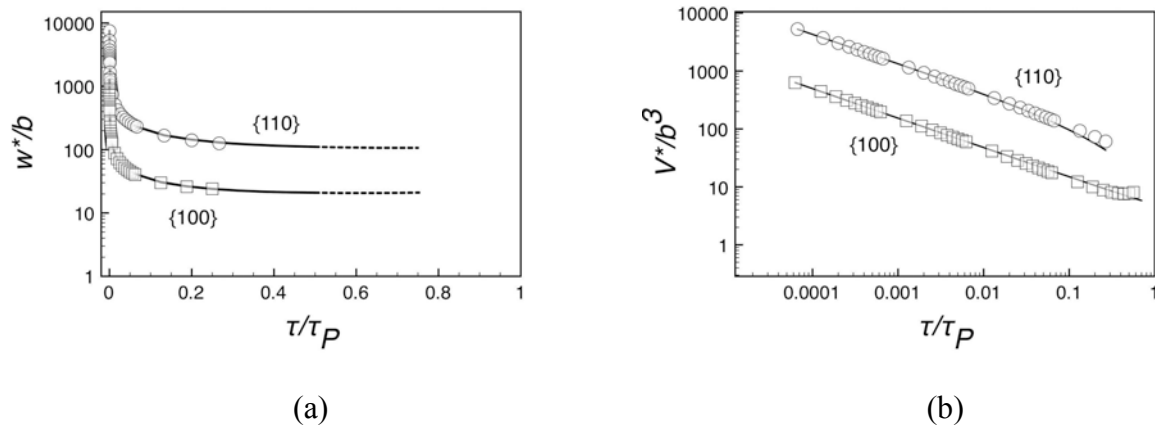

(a)   (b)

Fig. 4. Evolution of the kink pair shape as a function of stress for ½<110>{110} (open circles) and ½<110>{100} (open squares). (a) Activation volume h^*w^*b. Symbols correspond to the calculations whereas the line correspond to the extrapolation based on equation (5), using the fitted values of p and q listed in Table 1. (b) Variation in kink pair width w^* showing a strong decrease at low stress followed by a constant value w_c.
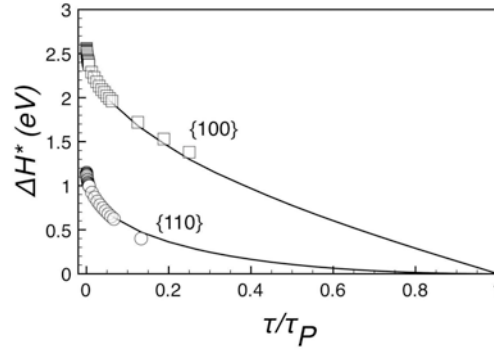
Fig. 5. Evolution of ΔH* as a function of stress (normalized to the Peierls stress). Symbols (open circles, slip system ½<110>{110}, open squares, slip system ½<110>{100}) correspond to the calculations whereas the line correspond to the extrapolation based on equation (4) and numerical values from Table 1.

3.3. From dislocation mobility to CRSS

In order to determine the CRSS in MgO, DD simulations have been performed below and above athermal temperature T_a. As mentioned in section 2, DD simulation relies on a velocity law which depends on the stress and on temperature. The latter dependency is very important below and is very weak above T_a, this is why the determination of the CRSS will thus be split into two parts. Above T_a, the dislocations have a high mobility and the macroscopic behaviour is controlled by dislocations-dislocations interactions. The flow stress is then essentially temperature independent. Below T_a the dislocation mobility is very low and the applied stress must increase to force dislocation motion, hence dislocation-dislocation interaction becomes negligible and the flow stress is controlled by the imposed strain rate. In order to run quantitative DD simulations, a reliable velocity law (function of temperature and stress) must then be defined.

3.3.1. Velocity laws

The velocity law defined in the DD simulation for screw dislocation segments is based on the nucleation and propagation of kink-pairs along a straight section of dislocation loops. Here, we assume that kink-pairs nucleation represents the controlling stage. Implicitly, this is equivalent to neglecting the potential second order lattice friction borne by edge type kinks created on a screw dislocation. This assumption is supported by the fact that Peierls stresses associated to edge dislocation in MgO [6, 31, 34] are significantly lower than those proposed here for screw dislocations. As a consequence, taking into account possible backward jumps of kink-pairs along a dislocation line, the velocity law takes the following form [62]:

$$v(\tau,T) = a' \upsilon_D b \frac{L}{2w^2} \left(\exp\left(-\frac{\Delta H^+(\tau)}{kT} \right) - \exp\left(-\frac{\Delta H^-(\tau)}{kT} \right) \right) \qquad (8)$$

Where ΔH^+ and ΔH^- correspond to the nucleation enthalpies of forward and backward jumps, a' and b correspond respectively to the width of the Peierls valley and to the Burgers vector. L is the length of a straight segment in the screw direction and w is the critical width of the kink-pair. Eq. (8) can be rewritten considering only the forward jump [78], leading to:

$$v(\tau,T) = a'\upsilon_D b \frac{L}{w^2} \exp\left(\frac{-\Delta H_0}{kT}\right) \sinh\left(\frac{\Delta H_0 - \Delta H^+(\tau)}{kT}\right) \qquad (9)$$

In this expression, ΔH^+ has formally the sense of ΔH^* calculated in the previous section with the kink-pair theory. ΔH^* and w depend on stress. However, as w evolves rapidly to reach an almost constant value w_c, we simplify Eq. (9) by using a constant w_c value, considering that the strongest stress dependence lies in the kink-pair nucleation enthalpy term ΔH^*. Finally, the expression of the velocity law for screw dislocations in MgO is:

$$v(\tau,T) = a'\upsilon_D b \frac{L}{w_c^2} \exp\left(\frac{-\Delta H_0}{kT}\right) \sinh\left(\Delta H_0 \left(1 - \left(1 - \left(\frac{\tau}{\tau_P}\right)^p\right)^q\right) \middle/ kT\right) \qquad (10)$$

for which all parameters are displayed in Table 1 for the glide planes {110} and {100}. 3D-DD simulations require to handle also the dynamics of the faster non-screw segments. The assessment of their velocity would ideally imply the same work as the one made for the screw dislocation character. However, on a technical point of view this effort is useless and a phenomenological approach is commonly adopted in the simulations of materials with lattice friction [79-82]. Non-screw dislocations being much faster than screws, they leave rapidly the sample, leaving long screw dislocations behind. This stage (called microplasticity) contributes to a negligible amount of strain. Further finite deformation is produced by screw dislocations which mobility controls plasticity. Therefore, precise value of non-screw segment velocity poorly affects the integration of a 3D dislocation dynamics. Hence, it is enough to consider that non-screw segments glide with the same type of velocity law as the screw segments, but without the segment length contribution appearing in Eq. (10) and multiplied by a factor K_v. $K_v = v_{edge}/v_{screw}$ is the velocity ratio between edge and screw segments. Taken larger than one, K_v speeds up the edge segments mobility at a given stress. Following previous work [79-82], we set a variation of K_v with temperature ranging from 10 000 at 0 K to 1 at T_a.

It is instructive to note that Eq. (10) leads for ½<110>{110} screw dislocations to a velocity of 10^{-6} m/s at ambient temperature under a typical stress of $\tau_P/10$ and to 0.1 m/s at 800 K. Alternatively, for ½<110>{100}, the calculated velocity with $\tau_P/10$ corresponds only to a few mm/s at 1200 K.

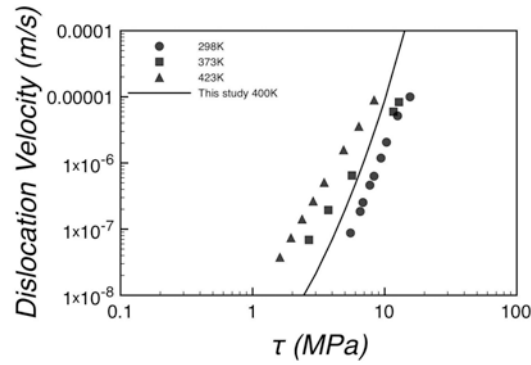**Fig. 6.** Dislocation velocity of the ½<110> screw dislocation used in this study (equation 10) compared with the average velocities of screw dislocations measured experimentally [16].

These values can be compared to the few existing values determined experimentally. In particular, Singh and Coble [16] measured, in a high-purity MgO single crystal, dislocation velocities in {110} which compare well with our calculations (Fig. 6). At higher temperature, we found that the velocity increases up to 10^{-1} m/s. This value is consistent with experimental velocities measured around 1000 K [11]. Regarding the velocity of non-screw segments, the velocity ratio K_v is usually adjusted to reproduce the anisotropic shape of observed dislocation loops. Unfortunately, few TEM micrographs are available in MgO on specimens deformed at low temperature (most of the TEM has been performed on specimens deformed in the high temperature creep regime, e.g. [10] or [83]). However, the few micrographs of specimens deformed at room temperature [84,85] suggest an anisotropic mobility between characters which supports the use of a large velocity ratio K_v at low temperature. Finally, above T_a, the fact that dislocation loops are curved, i.e. exhibit some line tension effect, suggest that screw and non-screw segments have comparable velocities, which justifies the choice of $K_v=1$ at T_a.

3.3.2. Flow stress below T_a

At low temperature, the critical shear stress is mainly controlled by the intrinsic mobility of screw dislocations which is governed by lattice friction. The strain-rate $\dot{\varepsilon}$ can thus be described by the Orowan law considering a distribution of mobile dislocations with a density ρ_m and an average velocity v (b is the Burgers vector):

$$\dot{\varepsilon} = \rho_m b v \tag{11}$$

In the thermal regime, all dislocation moving smoothly, one can assume that the mobile dislocation density is equal to the total density. The latter can be inferred from experiments,

with measured dislocation densities in the range 10^{11}-10^{12} m^{-2} [76] or 1-2 10^{12} m^{-2} in

specimens deformed at 1900°C under an applied stress of 60 MPa [8].

With this information, the CRSS of MgO was calculated with DD simulations by considering

a single dislocation of characteristic length $1/\sqrt{\rho}$ of 1 µm in a simulated volume of dimension

0.7 x 0.7 x 1.98 µm^3, corresponding to a dislocation density of 10^{12} m^{-2} (this value is used in

the whole study). The dislocation line is initially along a diagonal of the basis plane of the

simulated volume which is parallel to {001}. As an effect of periodic boundary conditions the

simulated screw segments is virtually infinite, this is why in the computation a maximum

straight screw length of 1 µm is applied to Eq. (10) during the simulation, i.e. 1 µm>L>0. We

carried out a series of compression test simulations at various temperatures to determine the

resulting flow stress at a constant strain-rate (10^{-4} s^{-1}). By varying the compression axis, the

dislocation can glide in either {100} or {110}. The results of the corresponding flow stresses

as a function of temperature are reported on Fig. 7.
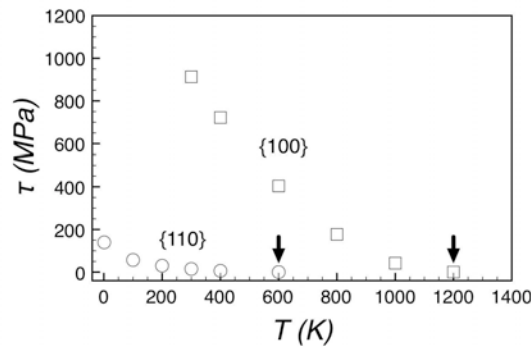

Fig. 7. Flow stress as a function of temperature in the thermal regime. Calculations, performed by DD simulations, are based on the Orowan law including dislocation velocities built in section 3.3.1. Stress values closed to zero are indicated by arrows and highlight the athermal threshold temperature T_a.

From this figure, the athermal threshold temperatures T_a is easily determined. Indeed, above a

temperature of 600 K for ½<110>{110} slip and of 1200 K for ½<110>{100} slip, the flow

stress has dropped to zero. This reveals that lattice friction is negligible at larger temperatures.

3.3.3 Flow stress above T_a

Above T_a lattice friction has vanished and the flow stress is governed by dislocations-

dislocations interactions which lead to a stress threshold τ_μ. In order to determine τ_μ for either

½<110>{110} and ½<110>{100}, we performed DD calculations with an initial dislocation

density of 10^{12} m^{-2} equally distributed on the six glide planes of each family. To prevent

artificial dislocation self-annihilations induced by PBC [66,79], the simulation volume was

rotated along the <111> axis and chosen as an orthorhombic cell of 10.7 x 11.7 x 10.8 μm^3 dimensions to ensure a mean free path of a few tens of micrometers before the occurrence of dislocation self-annihilation. We then performed multi-slip constant strain rate simulations (with solicitation axis [100] or [111] for activation of {110} or {100} slip systems) and measured the evolution of the flow stress as a function of strain. Two typical stress-strain curves are plotted on Fig. 8. Whatever the activated slip systems, one may note that a constant flow stress of around 10 MPa is reached for each slip system. Such value corresponds to a Taylor coefficient $\alpha = \tau/\mu b\sqrt{\rho}$ of 0.3 close to the value observed in most pure metals.
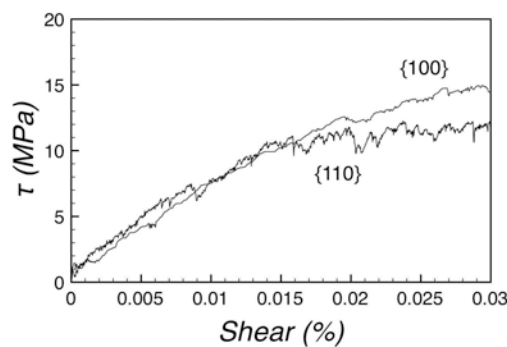

Fig. 8. Stress-strain curves recorded at 10^{-4} s^{-1} for a dislocation density of 10^{12} m^{-2}.

DD calculations have been performed at 1000 K and 1400 K for ½<110>{110} and ½<110>{100} respectively. The only constraint for the choice of these temperatures is that they are above T_a, since in this regime, varying T does not affect τ_μ. Following the same line, calculations have been performed using relatively high strain rate (i.e. 10^{-1} s^{-1} and 10^{-3} s^{-1} for respectively {110} and {100} simulations described above) for computation efficiency and with the same velocity law as for the low temperature regime. It is worth noticing that these choices does not influence τ_μ since we checked that the collective behaviour is controlled by forest interactions. In this regime, the flow stress is independent on the strain rate and on the velocity of individual dislocation (assuming the strain rate is low enough and the dislocation mobility is high enough to maintain a dynamics controlled by forest interaction, i.e. where dislocation gliding time is much smaller than their immobile time pinned at forest obstacles).

4. General discussion: comparison with experimental CRSS

4.1. Slip system ½<110>{110}

A lot of deformation experiments have been performed on MgO [9,11,13,86-89] which have produced data that can be compared with our calculations (see table 2 and Fig. 9). Fig. 9 shows a lot of dispersion in experimental data which comes from the presence of impurities as already pointed out by several authors [90-92]. Indeed, the strain-rate, which varies only within a moderate range in all these studies has little influence on the mechanical properties and will not be discussed further. Since MgO is an ionic compound, the influence of impurities is strongly related to their charges. Divalent cations seem to have little effect on dislocations and in crystals containing such impurities, dislocation glide is mostly governed by lattice friction at low temperature. When trivalent cations are predominant [89], both effect of lattice friction and impurities strengthening must be considered. Consequently, heat treatments under oxidizing or reducing atmospheres have implications on the mechanical properties in the presence of impurities like iron which can be either divalent or trivalent [90-92]. A critical comparison between our calculations and published data is then possible only if the influence of impurities (which are not taken into account in the model) is minimized. For this reason, the available information on impurity contents and heat treatments corresponding to the experiments reported on Fig. 9 are displayed in Table 2.

Reference	Label	Strain Rate (s^{-1})	Heat Treatment	Impurities (ppm)
[86]	A	4.4 10^{-4}	none	5600
	B	4.4 10^{-4}	1000°C - 1h	5600
[88]	A	4.4 10^{-4}	ND	290
	B	4.4 10^{-4}	ND	1390
[9]		1.3 10^{-5}	1250°C - 24h in air	239-244
[11]	A	4.1 10^{-4}	2000°C - 2h in argon gas	140
	B	4.1 10^{-4}	2000°C - 2h in argon gas	560
	C	4.1 10^{-4}	2000°C - 2h in argon gas + 1300°C - 24h in air	560
[13]		1 10^{-4}	ND	100
[89]		4.2 10^{-4}	ND	A few hundreds

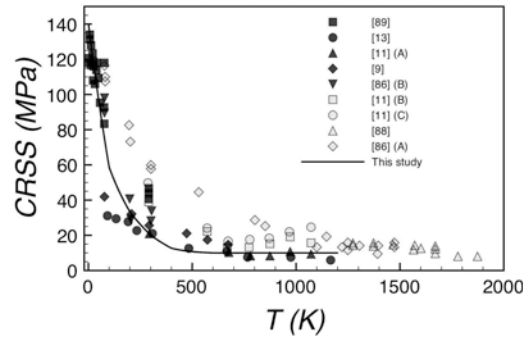**Table 2.** Summary of the experimental works used in this study for comparison with multiscale calculations.

Fig. 9. Critical resolved shear stress for ½<110>{110} slip systems. Comparison of the model (line) with experimental results (See information on these data in Table 2). A fair agreement is found with data corresponding to samples with the lowest impurity levels (black symbols).

On Fig. 9, our multiscale model assuming a dislocation density of 10^{12} m^{-2} is represented by the continuous line. Above T_a (i.e. 600 K), the flow stress is considered as controlled by forest hardening (CRSS=τ_u). Below T_a, the flow stress is controlled by the dislocation mobility and is predicted from the Orowan equation (Eq. (11)) in agreement with the simulation results reported in Fig. 7.

It is shown that a fair agreement is found with experimental results which correspond to the lowest impurity contents or to samples that have been annealed under reducing conditions (represented by black symbols on Fig. 9 for a sake of clarity). Fig. 9 shows also that the influence of impurity hardening becomes negligible at high temperature as well as at very low temperature where lattice friction clearly dominates.

4.2. Slip system ½<110>{100}

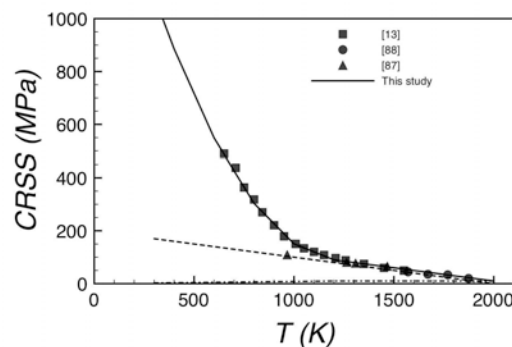**Fig. 10.** Critical resolved shear stress for ½<110>{100} slip system. The model reproduces the experimental results provided the addition of a solid-solution hardening contribution which is fitted between 1100 and 1800K.

Less data are available on this slip system, especially concerning the contribution of impurities. Fig. 10 shows that experimental data exhibits thermal activation of the flow stress until ca. 1800 K, i.e. well above the athermal temperature calculated with the mobility law deduced from the kink-pair model. To interpret this behaviour, we make the assumption that in this temperature range, the influence of impurity strengthening is still important. Following [17], we assume that this strengthening varies linearly with temperature and, assuming a linear composition of strengthening mechanisms, we adjust a linear contribution τ_i from the temperature range 1200-1800K. This impurity strengthening τ_i is supposed to contribute to the flow stress in the whole low-temperature domain. Our final model (again represented by a continuous line on Fig. 10) is made of the forest hardening contribution (τ_μ) above T_a, plus an impurity hardening (τ_i) and of lattice friction contribution (Fig. 7) below T_a. With this construction, our multiscale approach is found to account very well for experimental results. As is the previous slip system, it is shown that the contribution of impurity strengthening dominates in an "intermediate" temperature regime.

5. Conclusion

The goal of this work was to build a multiscale model for the plasticity of pure MgO that would not rely on parameters adjusted on experimental data. Instead, we rely on the properties of the core of screw ½<110> dislocations calculated with the PNG model which incorporates γ-surfaces calculated *ab initio* for the {110}, {100} and {111} planes. The PNG model gives access to the Peierls stress which is used to model thermal activation of glide in {110} and {100} based on a kink-pair model. The parameters of this thermal activation model are used to derive a velocity law for the screw dislocations in {110} and {100}. The collective response of the dislocation microstructure (in the form of the CRSS) is obtained from application of the Orowan equation below the athermal temperature T_a and from forest interactions above T_a. The present multiscale model rely on a few reasonable assumptions:

- accuracy of the description of the core of the ½<110> dislocation obtained from the PNG model
- relevance of the *elastic-interaction* model to describe kink-pair nucleation (considered as the rate-limiting mechanism)
- below T_a, the flow stress is governed by the mobility of screw dislocations and can be inferred by application of the Orowan equation.

- Above T_a, the flow stress is governed by forest interactions and can be modelled by DD.

- a dislocation density, here of 10^{12} m^{-2}, either taken from experimental data or eventually inferred from high-temperature flow stress calculated by DD simulations.

The good agreement observed between our model and available experimental data represent an indirect validation of these assumptions, although in some cases this might be just due to the weak sensitivity to a given parameter (this is the case for the dislocation density in the thermal regime for instance).

Comparison with experimental data has required to highlight the already well known influence of impurities. For glide on {110} the influence of impurities is extremely important below T_a, except may be very close to 0K where lattice friction becomes more important. On {100}, the role of impurities has been less discussed. Comparison with our model shows that their influence is dominant in the 1200-1800 K temperature range.

Having a model which does not depend on experimental parameters is of primary importance to extend the description to extreme conditions which are difficult to achieve in the laboratory. Since MgO is an important phase of the interior of the Earth, it is necessary to understand the influence of pressure on its plastic properties. The fact that dislocation core modelling relies on an accurate description of the electronic properties (through *ab initio* calculations of *γ*-surfaces) make it possible to incorporate the influence of pressure [6]. Combining this possibility and the present model opens the route for the modelling of plastic deformation of MgO in the conditions of the deep Earth.

References

[1] Stretton I, Heidelbach F, Mackwell S, Langenhorst F. Earth and Planetary Science Letters 2001; 194: 229.

[2] Merkel S, Wenk HR, Shu J, Shen G, Gillet P, Mao HK, Hemley RJ. J Geophysical Research 2002; 107: 2271.

[3] Li L, Weidner DJ, Chen J, Vaughan T, Davis M, Durham WB. J Applied Physics 2004; 95: 8357.

[4] Yamazaki D, Karato S. Physics of the Earth and Planetary Interiors 2002; 131: 251.

[5] Long MD, Xiao X, Jiang Z, Evans B, Karato S. Physics of the Earth and Planetary Interiors 2006; 156: 75.

[6] Carrez P, Ferré D, Cordier P. Modelling Simul Mater Sci Eng 2009; 17: 035010.

[7] Day RB, Stockes RJ. J Am Ceram Soc 1964; 47: 493.

[8] Huther W, Reppich B. Phil Mag 1973; 28: 363.

[9] Sinha MN, Lloyd DJ, Tangri K. Phil Mag 1973; 28: 1341.

[10] Clauer AH, Wilcox BA. J Am Ceram Soc 1976; 59: 89.

[11] Sato F, Sumino K. J Materials Science 1980; 15: 1625.

[12] Haasen P, Barthel C, Suzuki T. Choice of Slip System and Peierls Stresses in the NaCl Structure, in Suzuki H, Ninomiya T, Sumino K, Takeuchi S (Eds.). Dislocations in Solids; 1985.

[13] Barthel C. Plastiche Anisotropie von Bleisulfid und Magnesiumoxid, PhD Thesis, University of Gottingen; 1984.

[14] Foitzik A, Skrotzki W, Haasen P. Mater Sci Eng A 1989; 113: 399.

[15] Wicks BJ, Lewis MH. Phys. Stat. Sol. (a) 1971; 6: 281.

[16] Singh RN, Coble RL. J. Applied Physics 1974; 45: 981.

[17] Takeuchi S, Koizumi H, Suzuki T. Mater Sci Eng A 2009; 521-522: 90.

[18] Cai W, Bulatov VV, Chang J, Li J, Yip S. Dislocation core effects on mobility, in Nabarro FRN, Hirth JP (Eds.). Dislocations in Solids; 2004.

[19] Yamaguchi M, Vitek V. J Phys F: Metal Phys 1973; 3, 523.

[20] Xu W, Moriarty JA. Comp Materials Sci 1998; 9: 348.

[21] Schroll R, Vitek V, Gumbsch P. Acta Materiala 1998; 46: 903.

[22] Walker AM, Slater B, Gale JD, Wright K. Nature Materials 2004; 3: 715.

[23] Pizzagalli L, Beauchamp P. Phil Mag Lett 2004; 84: 729.

[24] Carrez P, Walker AM, Metsue A, Cordier P. Phil Mag 2008; 88: 2477.

[25] Groger R, Bayley AG, Vitek V. Acta Materiala 2008; 56: 5401.

[26] Joos B, Duesbery MS Phys Rev Lett 1997; 78: 266.

[27] Bulatov VV, Kaxiras E. Phys Rev Lett 1997; 78: 4221.

[28] Lu G, Kioussis N, Bulatov VV, Kaxiras E. Phil Mag Lett 2000; 80: 675.

[29] Schoeck G. Mater Sci Eng A 2005; 400-401: 7.

[30] Schoeck G. Acta Materiala 2006; 54: 4865.

[31] Woo CH, Puls MP. Phil Mag 1977; 35: 1641.

[32] Watson GW, Kelsey ET, Parker SC. Phil Mag A 1999; 79: 527.

[33] Walker AM, Gale JD, Slater B, Wright K. Phys Chem Chem Phys 2005; 7: 3235.

[34] Miranda CR, Scandolo S. Comp Phys Comm 2005; 169: 24.

[35] Seeger A, Schiller P. Acta Metallurgica 1962; 10: 348.

[36] Dorn JE, Rajnak S. Trans Met Soe AIME 1964; 230: 1052.

[37] Duesbery MS, Joos B. Phil Mag Lett 1996; 74: 253.

[38] Edagawa K, Koizumi H, Kamimura Y, Suzuki T. Phil Mag A 2000; 80: 2591.

[39] Joos B, Zhou J. Phil Mag A 2001; 81: 1329.

[40] Schoeck G. Phil Mag 2007; 87: 1631.

[41] Wang G, Strachan A, Cagin T, Goddard WAI. Phys Rev B 2003; 68: 224101.

[42] Domain C, Monnet G. Phys Rev Lett 2005; 95: 215506.

[43] Rodney D. Phys Rev B 2007; 76: 144108.

[44] Pizzagalli L, Pedersen A, Arnaldsson A, Jonsson H, Beauchamp P. Phys Rev B 2008; 77: 064106.

[45] Koizumi H, Kirchner HOK, Suzuki T. Acta metall mater 1993; 41: 3483.

[46] Koizumi H, Kirchner HOK, Suzuki T. Phil Mag A 1994; 69: 805.

[47] Carrez P, Ferre D, Cordier P. IOP Conf Series: Materials Science and Engineering 2009; 3: 012011.

[48] Kubin LP, Devincre B, Tang M. J of Computer-Aided Materials Design 1998; 5: 31.

[49] Madec R, Devincre B, Kubin LP. Phys Rev Lett 2002; 89: 255508.

[50] Madec R, Devincre B, Kubin LP, Hoc T, Rodney D. Science 2003; 301: 1879.

[51] Devincre B, Hoc T, Kubin LP. Science 2008; 320: 1745.

[52] Lu G. The Peierls-Nabarro Model of Dislocations: A venerable theory and its current development, in Yip S (Ed.). Handbook of Materials Modeling. Volume 1: Methods and Models; 2005.

[53] Ngan AHW. J Mech Phys Solids 1997; 45: 903.

[54] Ngan AHW, Zhang HF. J Applied Physics 1999; 86: 1236.

[55] Denoual C. Phys Rev B 2004; 70: 024106.

[56] Denoual C. Comp Methods Appl Mech Eng 2007; 196: 1915.

[57] Kresse G, Hafner J. Phys Rev B 1993; 47: 558.

[58] Kresse G, Furthmüller J. Comput Mat Sci 1996; 6: 15.

[59] Blöchl PE. Phys Rev B 1994; 50: 17953.

[60] Kresse G, Joubert D. Phys Rev B 1999; 59: 1758.

[61] Schoeck G. Phys Stat Sol 1965; 8: 499.

[62] Hirth JP, Lothe J. Theory of dislocations, John Wiley & Sons. Inc, New York; 1982.

[63] Carrez P, Ferré D, Denoual C, Cordier P. Scripta Materialia 2010; 63: 434.

[64] Devincre B, Kubin LP, Lemarchand C, Madec R. Mater Sci Eng A 2001; 309-310: 211.

[65] Cai W, Bulatov VV, Chang J, Li J, Yip S. Phil Mag 2003; 83: 539.

[66] Madec R, Devincre B, Kubin LP. (2004) On the use of periodic boundary conditions in dislocation dynamics, in Koizumi H, Yip S. (Eds.). IUTAM Symposium on Mesoscopic Dynamics of Fracture Process and Materials Strength, Kluwer Academic Publishers, NL-Dordrecht; 2004.

[67] Kubin LP, Canova G, Condat M, Devincre B, Pontikis V, Brechet Y. Solid State Phenom 1992; 23-24: 455.

[68] Devincre B. (1996) Meso-Scale Simulation of the Dislocation Dynamics, in E.H.O.K. et al., (Eds.). Computer simulation in Materials Science. NATO ASI Series; 1996.

[69] Devincre B, Kubin LP. Mater Sci Eng A 1997; 234-236: 8.

[70] Carrez P, Cordier P, Devincre B, Kubin LP. Mat Sci Eng A 2005; 400-401: 325.

[71] Moulin A, Condat M, Kubin LP. Acta Materiala 1997; 45: 2339.

[72] Tang M, Devincre B, Kubin LP. Acta Materiala 1998; 46: 3221.

[73] Chaussidon J, Robertson C, Rodney D, Fivel M. Acta Materiala 2008; 56: 5466.

[74] Caillard D, Martin JL. Thermally activated mechanism in crystal plasticity. Pergamon; 2003.

[75] Kocks UF. Argon AS, Ashby MF. Thermodynamics and kinetics of slip. Pergamon; 1975.

[76] Southgate PD, Mendelson KS, DePerro PL. J Applied Physics 1966; 31: 206.

[77] Philibert J. Glissement des dislocations et frottement de réseau, in Groh P, Kubin LP, Martin JL (Eds.). Dislocations et Déformation Plastique; 1979.

[78] Nabarro FRN. Phil Mag 2003; 83: 3047.

[79] Monnet G, Devincre B, Kubin LP. Acta Materiala 2004; 52: 4317.

[80] Durinck J, Devincre B, Kubin LP, Cordier P. American Mineralogist 2007; 92: 1346.

[81] Queyreau DJ, Monnet G, Devincre B. Int J Plasticity 2009; 25: 361.

[82] Naamane S, Monnet G, Devincre B. Int J Plasticity 2010; 26: 84.

[83] Groves GW, Kelly A. Proc R Soc Lond A 1963; 275: 233.

[84] Appel F, Bethge H, Messerschmidt U. Phys Stat Sol (a) 1976; 38: 103.

[85] Appel F, Bethge H, Messerschmidt U. Phys Stat Sol (a) 1977; 42: 61.

[86] Hulse CO, Pask JA. J Am Ceram Soc 1960; 43: 373.

[87] Hulse CO, Copley SM, Pask JA. J Am Ceram Soc 1963; 46: 317.

[88] Copley SM, Pask JA. J Am Ceram Soc 1965; 48: 139.

[89] Appel F, Wielke B. Mater Sci Eng 1985; 73: 97.

[90] Johnston WG, Gilman JJ. J Applied Physics 1959; 30: 129.

[91] Gorum AE, Luhman WJ, Pask JA. J Am Ceram Soc 1960; 43: 241.

[92] Srinivasan M, Stoebe TG. J Applied Physics 1970; 41: 3726.